Coherent electron emission beyond Young-type interference from diatomic molecules

H. Agueny,[1,2] A. Makhoute,[3] A. Dubois,[1] and J. P. Hansen[4]

[1]*Sorbonne Universités, UPMC University of Paris 06, CNRS, Laboratoire de Chimie Physique-Matière et Rayonnement, F-75231 Paris Cedex 05, France*

[2]*CONICET and Centro Atómico Bariloche, Comisión Nacional de Energía Atómica, Avenida E. Bustillo 9500, 8400 Bariloche, Argentina*

[3]*UFR de Physique du Rayonnement et des Interactions Laser-Matière, Faculté des Sciences, Université Moulay Ismail, B.P. 11201, Zitoune, Meknes, Morocco*

[4]*Department of Physics and Technology, Allégaten 55, University of Bergen, N-5007 Bergen, Norway*

(Received 16 March 2015; published 27 January 2016)

It has been known for more than 15 years that the differential cross section of electrons emitted from diatomic molecules during interaction with energetic charged particles oscillates as a function of electron momentum. The origin of the phenomenon is two-center interference, which naturally relates it back to the Young double-slit experiment. In addition to a characteristic frequency which can be described by lowest-order perturbation theories, the observation and origin of higher-order harmonics of the basic oscillation frequency has been much discussed. Here, we show that high harmonics of the fundamental Young-type oscillation frequency observed in electron spectra in fast ion-molecule collisions can be clearly exposed in numerical solutions of the time-dependent Schrödinger equation within a one-dimensional model. Momentum distribution of the ejected electron is analyzed and shows that the phenomenon emerges when the charged particle beam collides with diatomic molecules with substantial large internuclear distance. Frequency spectra from nonperturbative calculations for electron emission from Rb_2^+ and Cs_2^+ exhibit a pronounced high-order oscillation in contrast to similar close-coupling calculations performed on H_2 targets. The electron emission from these heavy molecules contains second- and third-order harmonics which are fully reproduced in an analytic model based on the Born series. Extending to triatomic molecular targets displays an increased range of harmonics. This suggests that electron emission spectra from new experiments on heavy diatomic and linear polyatomic molecular targets may provide a unique insight into competing coherent emission mechanisms and their relative strength.

DOI: 10.1103/PhysRevA.93.012713

I. INTRODUCTION

Few experiments have had a deeper footprint in the history of science than Young's double-slit experiment [1]. About 150 years later, Cohen and Fano [2] proposed a quantum-mechanical analog of this famous experiment where the light scattering from two slits is replaced by electronic photoionization from diatomic molecules. With the advance of new light sources, accelerators, and detector technologies since then, the coherent electron dynamics involving the two-center nature of the target has grown to be a hot topic within photon [3–5], electron [6,7], and ion impact [8] communities: Independent of the nature of the perturbing source, the diatomic target molecule generates electron emission spectra showing oscillatory structures due to two-center interference. The first experimental observations of the oscillations in the cross sections for electron emission induced in ion-molecule interactions, 60 MeV/nucleon Kr^{34+} colliding with H_2, were reported by Stolterfoht *et al.* [9] and sparked off intense further experimental and theoretical efforts to understand the complete nature of the phenomenon.

The basic oscillatory structure has been rather well described theoretically using a range of approaches, from first-order semiclassical treatment [8], distorted wave theories [7], and direct numerical solution of the time-dependent Schrödinger equation [10,11]. However, in the original experiment [9] and in a further investigation on Kr^{33+}-H_2 collisions [12], indications of additional oscillatory structures were observed. These were attributed to multiscattering phenomena of the electron within the molecule prior to emission. Independent measurements reported for electron emission by 1–5 MeV $H^+ + H_2$ collisions [13,14] showed a similar frequency doubling as well as additional even higher frequencies. An improved version of the original experiment of Stolterfoht *et al.* [9] was then carried out by Tanis *et al.* [15]. Their Fourier analysis of the spectrum did not exhibit evidence for high-frequency oscillations. More recent experiments with F^{9+} ions on H_2 [16] and H^+ on N_2 [17] have revealed signatures of frequency doubling indicating the observation of double-scattering mechanisms.

On the theoretical side, the distorted wave calculations [7] have in general improved the agreement with experiments as compared to the first-order semiclassical approach [8]. Second-order Born calculations, which result in frequency doubling, showed a qualitative improvement in comparison with results from H^+-H_2 collisions [18]. However, discrepancies remain at an absolute quantitative level. In contrast, time-dependent nonperturbative calculations in one-dimensional (1D), two-dimensional (2D) [10], and three-dimensional (3D) [11] models of highly charged ions colliding with H_2 could not identify any frequency doubling. The absence of signatures of frequency doubling in the nonperturbative calculations performed so far represents an unsettled issue.

It is the purpose of the present work to investigate the existence of second- and even higher-order oscillations in simple but robust nonperturbative simulations of model collisions between ions and diatomic systems. For this reason we consider a 1D collision system which to some extent can model a full 3D collision event with zero impact parameter and where both molecular orientation and direction of the ejected

electron are parallel to the projectile direction. The simplified 1D model approach is here relevant for the real 3D case in two aspects: Ionization occurs dominantly when the projectile is close to the target, regardless of the molecular alignment, and the additional features associated with the higher-frequency oscillations are independent of the ejected electron observation angle [12]. Apart from that a 1D model clearly has severe limitations. The main goal remains, nevertheless, to search for conditions for the absence or emergence of second-order frequencies in the electron emission spectrum of a full numerical solution of the time-dependent Schrödinger equation within a consistent model.

Our model, as well as its numerical implementation, is presented in the next section, which is followed by the discussion of the results and the comparison with an analytical model based on the Born series. The essence of the study is that clear signatures of higher harmonics on top of the dominant first-order "double-slit" oscillation emerge only for internuclear distances significantly larger than those of H_2. This is in agreement with the absence of visible second-order mechanisms in previous nonperturbative calculations for H_2 targets. We also propose new experiments with heavy molecular targets or even with polyatomic strings since these systems, according to our model, will magnify the high-order mechanisms. Atomic units, $e = m_e = \hbar = 4\pi\varepsilon_0 = 1$, are applied unless otherwise stated.

II. THEORETICAL MODEL AND NUMERICAL SIMULATIONS

Within the semiclassical approach we solve the 1D time-dependent Schrödinger equation (TDSE)

$$\left[H_e(x,t) - i\frac{\partial}{\partial t}\right]\psi(x,t) = 0 \tag{1}$$

for a diatomic molecule with fixed internuclear distance, keeping otherwise the projectile energy and charge within the parameter region of previous experiments and calculations [19]. The electronic Hamiltonian $H_e(x,t)$ is expressed as

$$H_e(x,t) = -\frac{1}{2}\frac{d^2}{dx^2} + V(x_a) + V(x_b) + V_p(x,t), \tag{2}$$

where $x_{a/b} = x - X_{a/b}$ and $X_{a/b}$ locates the target nucleus a/b so that the internuclear distance is $R_{ab} = X_b - X_a$. $V(x_{a/b})$ is the interaction potential between the electron and each target nucleus and takes the form

$$V(x) = -\frac{1 + (Z-1)e^{-c_1|x|} + c_2 x e^{-c_3|x|}}{\sqrt{x^2+\alpha}}, \tag{3}$$

where Z is the nuclear charge and c_1, c_2, c_3 are empirical parameters, which have been chosen as in [20]. $V_p(x,t)$ is the Coulomb interaction between the target electron and the projectile of charge Z_p [located at $X(t) = vt$ with v the relative target-projectile velocity]:

$$V_p(x,t) = -\frac{Z_p}{\sqrt{[x - X(t)]^2 + \beta}}. \tag{4}$$

Furthermore, for both potentials V and V_p, we use the regularized Coulomb soft-core form in terms of the parameters α and β, respectively. Here $\beta = 2.0$ and $\alpha = 0.64$ (0.85) have been chosen to reproduce the ionization energies 0.1909 a.u. (0.1536 a.u.) for $Rb_2{}^+$ (Rb) [20,21].

Equation (1) is solved by expanding the time-dependent wave function on a basis of Lagrange functions

$$\psi(x,t) = \sum_{n=1}^{N} a_n(t) f_n(x), \tag{5}$$

where a_n is the expansion coefficient and f_n represent the Lagrange functions which are expressed on a set of N orthonormal basis functions $\varphi_k(x)$ [22]:

$$f_n(x) = \lambda_n^{1/2} \sum_{k=1}^{N} \varphi_k^*(x_n)\varphi_k(x). \tag{6}$$

In such a (Lagrange-mesh) method, the mesh is defined by a set of N points x_n (spanning a large region of space, the box) and weights λ_n, connected with the Gauss quadrature scheme at N points:

$$\int_a^b F(x)dx \approx \sum_{k=1}^{N} \lambda_k F(x_k). \tag{7}$$

Within the framework of this approximation, the Lagrange functions $f_n(x)$ satisfy [22]

$$f_n(x_m) = \lambda_n^{-1/2}\delta_{nm} \tag{8}$$

and the orthonormality condition

$$\int_a^b f_n^*(x) f_{n'}(x)dx = \delta_{nn'}. \tag{9}$$

Once the Lagrange functions are constructed, the matrix related to the Laplacian of Eq. (2) can be expressed analytically; those representing the potential terms are diagonal and can be evaluated directly on the mesh points x_n. The Lagrange-mesh method has been shown to be very efficient with high accuracy for many kinds of eigenvalues problems. Additionally, its application for solving the time-dependent problems was reported by Melezhik and Baye [23], where its fast convergence is observed and discussed.

The variational basis functions φ_k used in the present work are defined as

$$\varphi_k(x) = \sqrt{2}\sin(k\pi x) \tag{10}$$

and the Lagrange functions can be deduced from Eqs. (6) and (10) [24]. Then the kinetic energy operator matrix has the compact expression

$$T_{nm} = \begin{cases} (-1)^{n-m}\frac{\pi^2}{4}\left\{\frac{1}{\sin^2(\frac{n-m}{2}\frac{\pi}{N+1})} - \frac{1}{\sin^2(\frac{n+m}{2}\frac{\pi}{N+1})}\right\}, & n \neq m \\ \frac{\pi^2}{4}\left\{\frac{1+2(N+1)^2}{3} + \frac{1}{\sin^2(m\frac{\pi}{N+1})}\right\}, & n = m. \end{cases} \tag{11}$$

Using this method the amplitudes $a_n(t)$ of Eq. (5) are propagated numerically using a predictor-corrector algorithm with an adaptive step scheme due to Shampine and Gordon [25]. After propagation the ionization wave function ϕ_{ioni} is extracted by projecting out the contribution of bound states of the diatomic target from the total scattering wave

function

$$\phi_{\rm ioni}(x) = \psi(x,t\to\infty) - \sum_n \int \psi_n^*(x')\psi(x',t\to\infty)dx'\psi_n(x), \quad (12)$$

where the sum runs over the important target bound states ψ_n. In the present case this sums covers the three lowest bound states to reach sufficient convergence of the results. The results presented in the following section are carefully checked for convergence concerning box sizes, mesh sizes, and propagation times. We note that a mask function was used to remove reflections from box boundaries, avoiding spurious perturbations of the inner part of the wave function at the cost of a weak probability leak (from less likely fast electrons). In closing, we emphasize that, contrary to perturbative low-order treatments, our close-coupling calculations do not exclude any mechanisms or processes which can give rise to a specific final state.

III. RESULTS AND DISCUSSION

The processes to be discussed in the following are schematically displayed in Fig. 1. From top to bottom the first-, second-, and third-order scattering mechanisms leading to coherent electron emission from nucleus a (left) and nucleus b (right) are illustrated. The top diagram represents first-order effect: Here the electron is ejected from either atom a or atom b directly to the continuum with a final momentum vector $\vec{k}_f$. The first-order treatment of ion-molecule scattering gives an expression for the oscillations very similar to that obtained by Cohen and Fano in the case of photoionization [2,8]. When performing a first-order analysis within a 1D model, the scattering wave can be expressed as a coherent superposition of two plane waves of fixed momentum p_x emitted from both centers (see [10]):

$$\phi^{\pm}_{\rm ioni}(p_x) \propto e^{\pm i|p_x|(x-R_{ab}/2)-iEt} + e^{\pm i|p_x|(x+R_{ab}/2)-iE(t-\delta t)}, \quad (13)$$

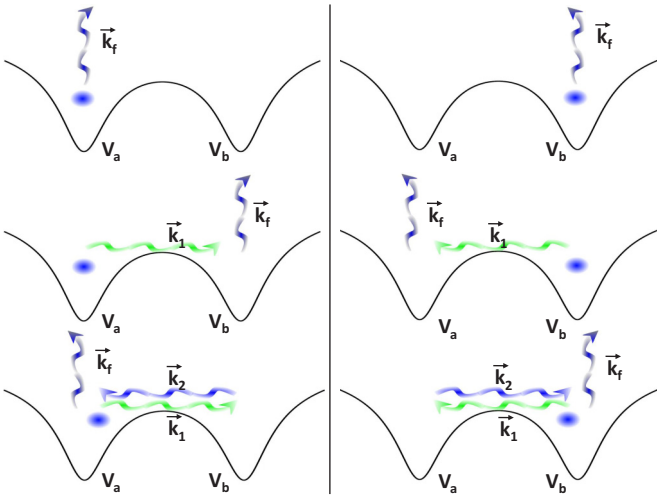

FIG. 1. Diagrams showing interference mechanisms of increasing order: (top) first order, (middle) second order, and (bottom) third order.

where $\pm$ refers to forward (+) or backward (−) electron ejection. The latter expression can be brought to the simple form

$$|\phi^{\pm}_{\rm ioni}(p_x)|^2 \propto 1 + \cos(\pm|p_x|R_{ab} + E\delta t), \quad (14)$$

where E is the energy of the ejected electron and $\delta t = R_{ab}/v$ corresponds to the phase shift between the waves emitted by a and b. In the high impact velocity domain considered in the following the phase has a rather small effect but it explains the asymmetry between forward and backward scattering [10].

The second-order effect is schematically represented in the middle panel. This is a contribution from two separate processes: The primary electronic wave stemming from the center a (b) propagates along the interatomic axis with the electron momentum $\vec{k}_1$ (having the energy E_1) and then it gets scattered off by the center b (a) with the final momentum vector $\vec{k}_f$. Finally, an example of a third-order process is given in the bottom panel: It contains an additional elastic intramolecular scattering event of the active electron which at the point of returning to the origin nucleus will scatter off with the final momentum $\vec{k}_f$.

In order to test our numerical calculations, we revisit the H^+-H_2 ($R_{ab} = 1.4$ a.u.) collision to investigate high-order interferences of the electron prior emission. The process under consideration is dealt with in the nonperturbative approach presented above. As in the previous calculations [10], we consider high impact energy collisions (∼63 MeV/nucleon, i.e., $v \sim 50$ a.u.).

The convergence of the results constitutes a crucial step for the meaningful analysis of the (tiny) oscillations superimposed on the clear Young-type (first-order) ones which may be present in the momentum distribution of the ejected electron [i.e., the squared modulus of the Fourier transform of the ionization wave function of Eq. (12) to the momentum space] shown in Fig. 2(a). We have therefore performed extensive numerical tests and we are confident on the convergence of the data presented below with respect to the effects that we want to analyze: These data stem from calculations with $N = 32\,768$ mesh points within a box of size 6400 a.u. and a propagation time $t_f = 200$ a.u.

As observed in [10], the results of Fig. 2(a) demonstrate quantum interferences related to the coherent electron emission induced by a proton in the vicinity of the two atomic centers of H_2, as described in Fig. 1 (top).

The frequency spectra resulting from Fourier transformation of the ratio between the momentum distributions in backward scattering of H_2 and H after the collision, i.e., at the time $t_f = 200$ a.u., are shown in Fig. 2(b). The single peak in the spectrum reveals the primary frequency of Young-type interference, in agreement with Eq. (14). Apart from this structure, no additional structure in frequency spectrum can be observed.

A critical parameter for the second- and higher-order mechanisms to be pronounced is the internuclear distance, R_{ab}; cf. Eq. (14). As $R_{ab} = 1.4$ a.u. for H_2 compares to the de Broglie wavelength of the emitted electron in the observed range of electron velocities (1.5–6 a.u.), we may suspect that the dimension of the hydrogenic molecular target is too small to accompany significant (observable) double-scattering events.

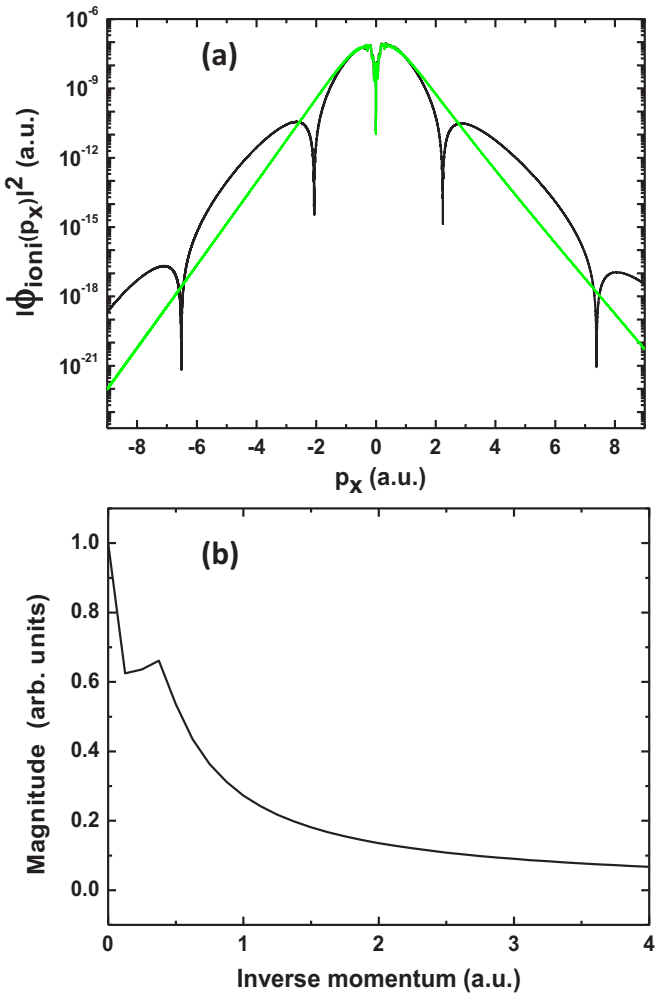

FIG. 2. 1D calculations for electron emission from H_2 by 63 MeV/nucleon H^+ impact. (a) Momentum distribution of the ejected electron:; black line, H^+-H_2; green line, H^+-H. (b) Magnitude of the Fourier transform of the ratio of distributions for backward scattering.

The situation could be changed by analyzing oscillations at higher electron energies but here ionization is weak, with a four-order-of-magnitude decrease when scanning up to a few hundred eV [9]: First-order interferences can hardly be observed in experimental spectra and data from simulation may reach background numerical noise so that the analysis of additional oscillations may become questionable. The remaining alternative is to consider molecules with larger internuclear distance.

Therefore, we consider the solution of the TDSE for a molecular target with significantly larger internuclear distance. In Fig. 3(a) we show the momentum distribution of the ejected electron as a function of time and momentum in the forward and backward direction for collision between a proton and the Rb_2^+ molecular ion, characterized by $R_{ab} = 9.2$ a.u. In Fig. 3(b) we show the corresponding results from a "2Rb" pseudomolecular model where the amplitudes from two ion-atom calculations are coherently added and shifted in amplitude, by the same interatomic distance. Although both calculations exhibit the characteristic Young-type oscillatory

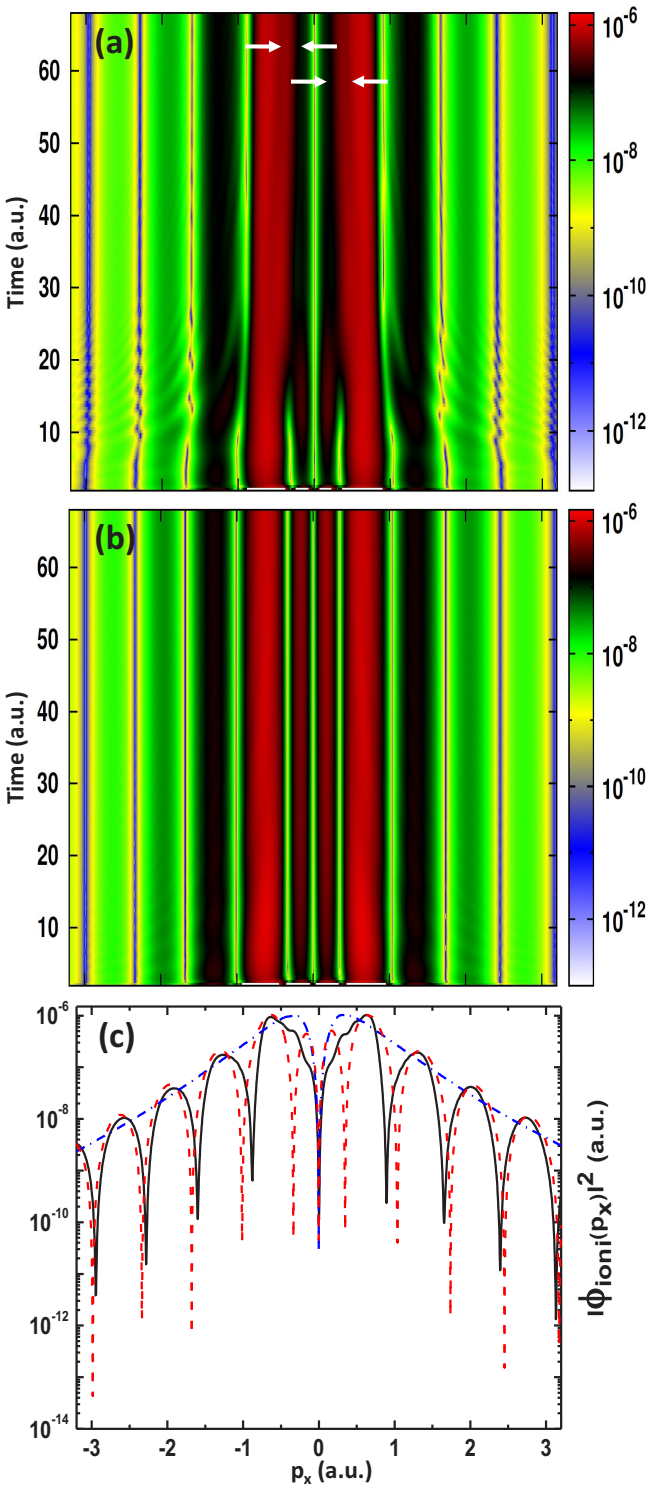

FIG. 3. Momentum distribution as a function of time and ejected electron momentum following 63 MeV/nucleon ($v \approx 50$ a.u.) H^+-Rb_2^+ collisions (a) from the model taking into account molecular effects for the target and (b) from the 2Rb model, i.e., the coherent sum of ionization wave functions from two independent Rb atoms. In both models, the internuclear distance is fixed at $R_{ab} = 9.2$ a.u. (c) 1D momentum distribution of the ejected electron at the time of propagation $t_f = 82$ a.u.: black line, H^+-Rb_2^+; blue dash-dotted line, H^+-Rb; red dashed line, H^+-2Rb.

momentum distributions, we note some distinct molecular effects, in particular at low momenta. In the case of Rb_2^+, we observe the extinction of the first minimum located around $|p_x| \simeq 0.3$ a.u. after 15 a.u. collision time. We note that a similar suppression has been observed experimentally in the ionization of N_2 by 1–5 MeV/nucleon protons [17]. These minima remain present in the 2Rb model even at long propagation times. Moreover, an additional tiny pattern can be seen on both sides of the central line for Rb_2^+, as indicated by the white arrows, while such side structures do not appear for 2Rb.

The observed differences in Figs. 3(a) and 3(b) become obvious when the electron energy spectra are plotted after the collision; see Fig. 3(c). The full molecular treatment displays additional structures at low momenta while the momentum distribution from the two-atom model becomes similar only at high electron energies.

To analyze the interference pattern with higher visibility, we plot the momentum distributions of the ejected electron of the dimer Rb_2^+ divided by those of the monomer Rb. The results are presented in Fig. 4(a) together with the two-independent-center 2Rb model and compared with the first-order oscillations given by Eq. (14). The strongest departure from the first-order theory is seen to be most pronounced at small backward and forward momenta in the full Rb_2^+ calculation. Additionally, the results reveal a small but clear asymmetry between forward-backward emission, in concordance with Eq. (14).

When analyzing the frequency distribution, by taking the Fourier transform of the distribution ratio [26] displayed in Fig. 4(a) for backward momenta, we observe in Fig. 4(b) clear second and third harmonics of the fundamental frequency from the full molecular treatment. In contrast, the two-atom model displays only the characteristic first-order frequency, i.e., that of the cosine function of Eq. (14).

Let us now compare these results with the calculated spectra from selected first-, second-, and third-order Born series amplitudes. The full transition amplitude up to second order can be written as

$$a(k_1,k_f) = a^{(1)}(k_f) + a^{(2)}(k_1,k_f), \tag{15}$$

where the first term corresponds to the first-order amplitude; its expression is given by

$$a^{(1)}(k_f) \sim \int_{-\infty}^{\infty} dt e^{i\Delta E t} \langle \psi_{k_f} | V_p(t) | \psi_i \rangle. \tag{16}$$

The contribution of the second-order amplitude contains elements on the form [27] $a^{(2)}(k_f) = \int d^3k_1 [a^{(2),+}(k_1,k_f) + a^{(2),-}(k_1,k_f)]$, where the two partial amplitudes relate to forward (+) and backward (−) interatomic scattering and describe precisely the mechanisms sketched in Fig. 1 (middle). It can be expressed as

$$a^{(2),\pm}(k_1,k_f) \sim \int_{-\infty}^{\infty} dt_2 e^{i\Delta E_2 t_2} \langle \psi_{k_f} | V_s(x) | \psi_{k_1}^{\pm} \rangle \times \int_{-\infty}^{t_2} dt_1 e^{i\Delta E_1 t_1} \langle \psi_{k_1}^{\pm} | V_p(t_1) | \psi_i \rangle, \tag{17}$$

where $V_s(x) = V(x_a) + V(x_b)$ describes the electron target. ΔE_i $(i = 1,2)$ is the energy transfer to the electron.

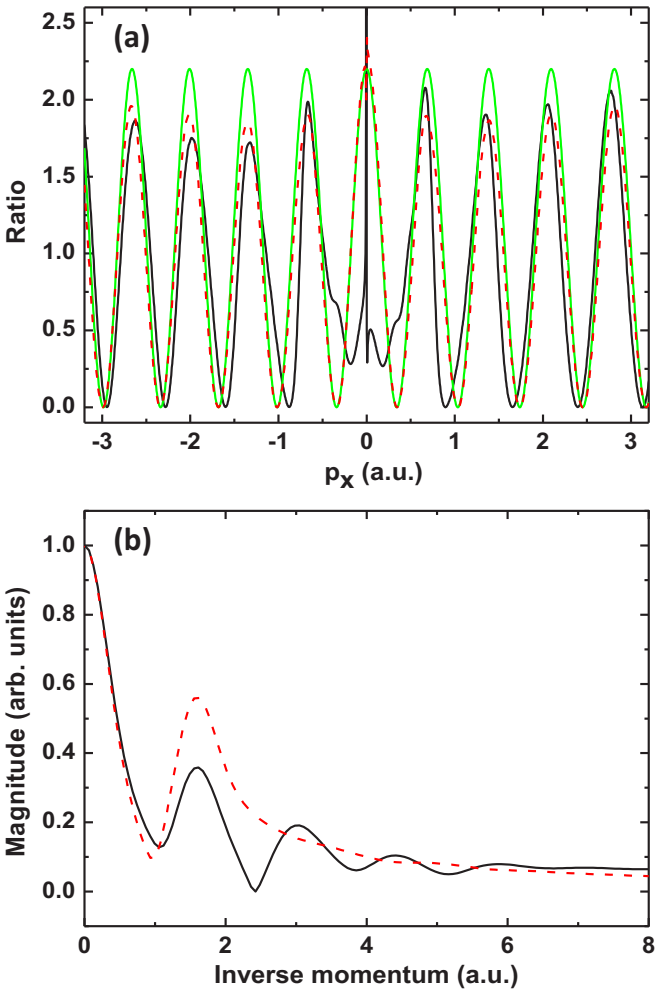

FIG. 4. Electron emission in 63 MeV/nucleon H^+-Rb_2^+ collisions. (a) Ratio of the momentum distributions for molecular (Rb_2^+) and atomic (Rb) targets: black line, full calculation; red dashed line, results from the two-independent-atoms (2Rb) model; green (light gray) line, model of the first order given by Eq. (14). (b) Magnitude of the Fourier transform of the distribution ratios for backward scattering, convoluted with Gaussian functions [black and red dashed lines, same as in (a)].

To evaluate the amplitude in Eqs. (16) and (17), we assume that the terms V_p in V_s are screened Coulomb (or Gaussian, see below) potentials describing approximately the interaction between the electron and the two centers of the molecular target [see Eq. (3) for the form used in the numerical calculations]. The perturbation V_p is set constant, and the initial state is expressed as a linear combination of two atomic centers a and b, respectively,

$$\psi_i = N(\varphi(x_a) + \varphi(x_b)), \tag{18}$$

where N is a normalization factor. The final and intermediate wave functions for electrons of momenta k_f and k_1, respectively, are approximated by plane waves and can be written as

$$\psi_{k_f} = (2\pi)^{-3/2} e^{ik_f x} \tag{19}$$

and

$$\psi_{k_1}^{\pm}(x) = (2\pi)^{-3/2} e^{\pm i k_1 x}. \tag{20}$$

This plane-wave approximation allows us to get a simple analytic expression for the amplitudes in Eqs. (16) and (17); after integration over the time t and the electronic coordinate x, we thus get, for the first-order amplitude,

$$a^{(1)}(k_f) \sim \cos(k_f R_{ab}/2)\hat{\varphi}(k_f), \tag{21}$$

and for the contribution of the second-order amplitude,

$$a^{(2),\pm}(k_1,k_f) \sim \cos(Q_{\pm} R_{ab}/2)\cos(k_1 R_{ab}/2)\hat{V}(Q_{\pm})\hat{\varphi}(k_1), \tag{22}$$

where the momentum transfer $Q_{\pm} = k_f \pm k_1$,

$$\hat{V}(Q_{\pm}) = \int dx_{a/b} V(x_{a/b}) \exp(-i Q_{\pm} x_{a/b}), \tag{23}$$

and

$$\hat{\varphi}(k_{1/f}) = \int dx_{a/b} \varphi(x_{a/b}) \exp(-i k_{1/f} x_{a/b}). \tag{24}$$

In order to perform analytically the integrals in Eqs. (23) and (24), we make use of a Gaussian form to describe both the electron-target interaction and the initial state. These approximations lead to an analytic expression for the contribution of the second-order scattering probability term, $|a^{(2)}|^2 \sim |a^{(2),+}|^2 + |a^{(2),-}|^2 + 2Re(a^{(2),+,*}a^{(2),-})$, where the last term represents the interference between the two processes. Considering elastic processes only in the continuum ($k_1 = k_f$), the probability takes then the form

$$\begin{aligned} |a^{(2)}(k_f)|^2 \sim |a|^2 [3 &+ 3\cos(k_f R_{ab}) + 4\cos(k_f R_{ab}) \\ &+ 6\cos(k_f R_{ab})\cos(k_f R_{ab}) + \cos(2k_f R_{ab}) \\ &+ \cos(k_f R_{ab})\cos(2k_f R_{ab})]. \end{aligned} \tag{25}$$

This expression contains the fundamental frequency, the first harmonics in the second and third term, a component with the second harmonics, and finally a third harmonics originated from the interference between the final and intermediate waves. Therefore, the full second-order scattering probability is $|a|^2 = |a^{(1)}|^2 + |a^{(2)}|^2 + 2Re(a^{(1),*}a^{(2)})$, where the last term represents the interference between the first-order amplitude and the contribution of the second-order amplitude. In the following, we neglect this term, and only the contribution of the second-order amplitude is analyzed. This is valid only as long as the nature and the origin of the high-order oscillations are explored.

In Fig. 5 the Fourier transform of expression (25) is plotted together with the similar relation for the contribution of the third-order probability. We note that the third-order term gives an additional fourth harmonics of the basic oscillation frequency. These harmonics are seen to be in complete concordance with the dominant frequencies of the TDSE results for the Rb_2^+ target. The close agreement between our analytical Born series model and the molecular TDSE calculation demonstrates the origin of the calculated oscillations in the spectrum.

The key to the emergence of clear harmonics has been the substitution of the "standard" target molecule H_2 with a heavier molecule of much larger internuclear separation. In

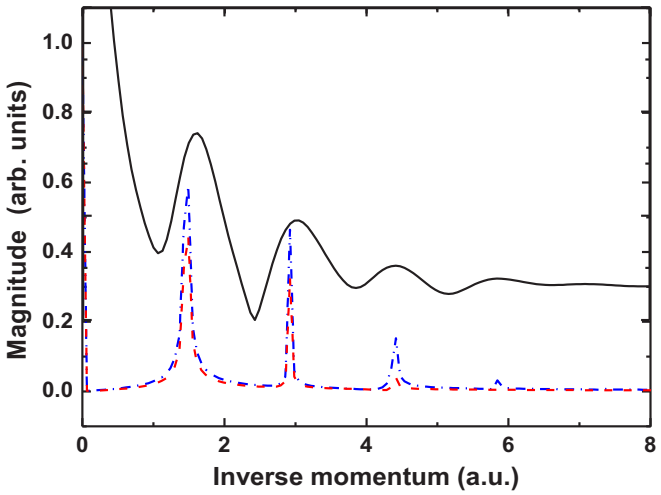

FIG. 5. Frequency distributions of the second- (red dashed curve), Eq. (25), and third-order (blue dash-dotted curve) Born amplitudes with selected intermediate states with $k_1 = k_2 = k_f$; cf. Fig. 1. The frequency distributions stemming from the TDSE from the 63 MeV/nucleon H^+-Rb_2^+ system (same as in Fig. 4) are shown by a black line with an offset.

Fig. 6 we show the results of calculations for the additional molecules H_2+ ($R_{ab} = 2.0$ a.u.) and Cs_2^+ ($R_{ab} = 10.1$ a.u.). The results for the latter show again distinct signatures of high-order oscillations at slightly higher frequencies than in Rb_2^+, as expected. In contrast only the basic frequency appears for the H_2^+ molecular ion.

In order to support our suggestions regarding the significant role of the molecular internuclear distance to highlight the predicted high-order interferences, we have performed additional calculations for four values of R_{ab} (1.4, 5, 6, and 7 a.u.). In these calculations, we have used a short range potential with a Gaussian form $[-\exp(-\alpha|x - R_{ab}/2|^2) - \exp(-\alpha|x - R_{ab}/2|^2]$ to describe the electron-molecule interaction. Here the nuclear charge of the molecular target is fixed

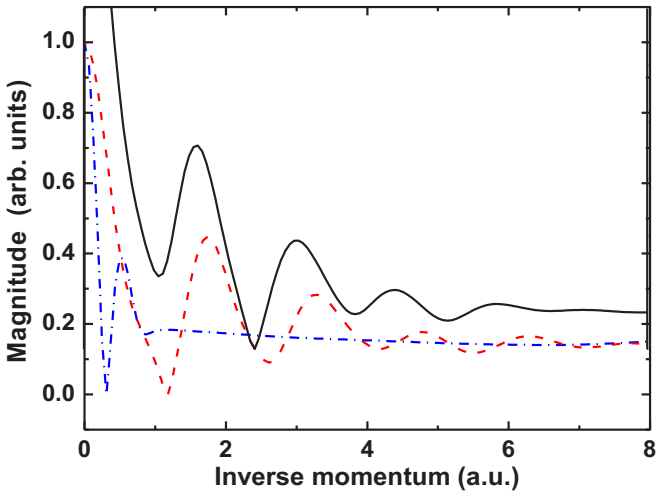

FIG. 6. Frequency distributions from calculations for 63 MeV/nucleon H^+ impact on H_2^+ (blue dash-dotted curve), Cs_2^+ (red dashed curve), and Rb_2^+ (black curve with offset).

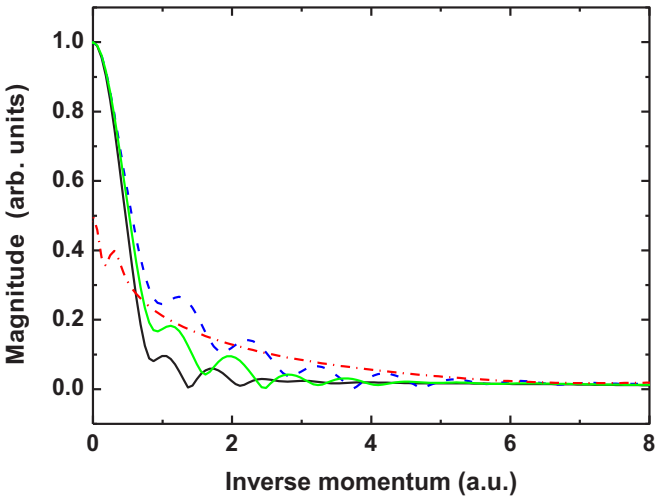

FIG. 7. Frequency distributions of the higher-order harmonics stemming from the TDSE, for four molecular internuclear distances R_{ab} at 63 MeV/nucleon proton impact. For all R_{ab}, we use the same potential, which is given in a Gaussian form, to describe the electron-molecule interaction: $R_{ab} = 1.4$ a.u. (red dash-dotted curve), $R_{ab} = 5$ a.u. (black curve), $R_{ab} = 6$ a.u. (green curve), and $R_{ab} = 7$ a.u. (blue dashed curve).

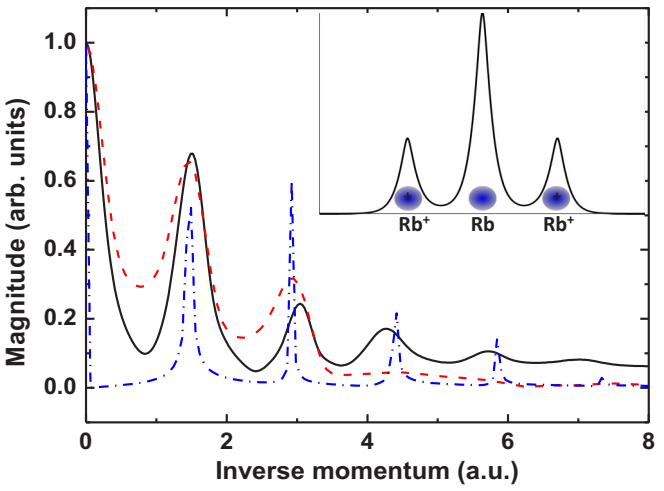

FIG. 8. Frequency distributions from calculations of H^+-$Rb_3{}^{2+}$ (black curve) and H^+-3Rb (red dashed curve) collisions compared with the Fourier spectrum from the second Born model of Eq. (25) applied to a trimer (blue dash-dotted curve). Inset: Initial electronic probability density vs spatial coordinate x ($|x| < 20$ a.u.).

as for H_2^+ ($Z = 1$ for each center), and the only parameter to be varied is the molecular internuclear distance. This allows us to rule out any effect due to the nuclear charge to observe high-order oscillations. The results, displayed in Fig. 7, show that the high-order oscillations appear as the internuclear distance becomes about four to five times the one of H_2. Once again, the observed frequencies of the high-order harmonics agree with second- and third-order Born calculations.

Finally we point out that high-order emission harmonics can become even more pronounced for similar linear three-center molecules (or longer chains). In the TDSE results for the Rb_3^{2+} trimer shown in Fig. 8 one can observe up to five distinct harmonics due to an interplay between a much larger range of scattering possibilities from three centers. The "3Rb" model, obtained by adding three independent atomic amplitudes at three fixed atomic distances of 9.2 a.u., exhibits only the two basic frequencies expected. Again, the second-order model applied to the trimer reproduces the spectrum.

IV. CONCLUSIONS

In this work we have demonstrated high-order interference in coherent electron emission from dimers induced by fast ions based on TDSE 1D calculations. The results stemming from this approach are supported by an analysis in terms of second- and third-order Born series. The main observation is that harmonics of the basic frequency $R_{ab}/2\pi$ may appear when the internuclear distance becomes sufficiently large, i.e., four to five times that of H_2, so that electronic wave packets between the target centers can develop, resulting in multiscattering processes. This is in agreement with a naive picture of the dimension of the electron de Broglie wavelength as compared to the molecular internuclear distance. The high harmonics are clear signatures of coherent contributions from second- and higher-order processes to the final electron emission amplitude. Extension to triatomic linear molecules with corresponding large distances reveals additional and stronger harmonics.

In addition to an extension of this work towards a full 3D treatment, the present results call for more experimental work towards systematic investigations of various heavy diatomic or polyatomic linear molecules and molecular ions. If experiments can detect a pronounced spectrum of high harmonics it may lead to new applications of electron emission interference spectroscopy, such as extended x-ray absorption fine structure spectroscopy [28] in solid-state physics. The fundamental aspects of such experiments will not cast light on the "eternal" quantum mechanics dilemma of which slit the particle goes through, but they may display with clarity the more precise question regarding which processes take place before the particle emerges from the two slits.

ACKNOWLEDGMENTS

This work has been supported by the EU Seventh Framework Programme under Grant Agreement No. PIRSES-GA-2010-269243 and the Norden Top Researcher Initiative. One of the authors (H. A.) would like to thank Dr. N. Sisourat for fruitful discussions.

[1] T. Young, Philos. Trans. R. Soc. London **94**, 1 (1804).
[2] H. D. Cohen and U. Fano, Phys. Rev. **150**, 30 (1966).
[3] R. Della Picca, P. D. Fainstein, M. L. Martiarena, N. Sisourat, and A. Dubois, Phys. Rev. A **79**, 032702 (2009).

[4] D. I. R. Boll and O. A. Fojón, Phys. Rev. A **90**, 053414 (2014).
[5] X.-J. Liu, Q. Miao, F. Gel'mukhanov, M. Patanen, O. Travnikova, C. Nicolas, H. Ågren, K. Ueda, and C. Miron, Nat. Photonics **9**, 120 (2015).
[6] Z. N. Ozer, H. Chaluvadi, M. Ulu, M. Dogan, B. Aktas, and D. Madison, Phys. Rev. A **87**, 042704 (2013).
[7] M. F. Ciappina, O. A. Fojón, and R. D. Rivarola, J. Phys. B **47**, 042001 (2014).
[8] L. Nagy, L. Kocbach, K. Pora, and J. P. Hansen, J. Phys. B **35**, L453 (2002).
[9] N. Stolterfoht, B. Sulik, V. Hoffmann, B. Skogvall, J. Y. Chesnel, J. Rangama, F. Frémont, D. Hennecart, A. Cassimi, X. Husson, A. L. Landers, J. A. Tanis, M. E. Galassi, and R. D. Rivarola, Phys. Rev. Lett. **87**, 023201 (2001).
[10] N. Sisourat, J. Caillat, A. Dubois, and P. D. Fainstein, Phys. Rev. A **76**, 012718 (2007).
[11] L. Sælen, T. Birkeland, N. Sisourat, A. Dubois, and J. P. Hansen, Phys. Rev. A **81**, 022718 (2010).
[12] N. Stolterfoht, B. Sulik, B. Skogvall, J. Y. Chesnel, F. Frémont, D. Hennecart, A. Cassimi, L. Adoui, S. Hossain, and J. A. Tanis, Phys. Rev. A **69**, 012701 (2004).
[13] S. Hossain, A. L. Landers, N. Stolterfoht, and J. A. Tanis, Phys. Rev. A **72**, 010701 (2005).
[14] S. Hossain, N. Stolterfoht, and J. A. Tanis, Nucl. Instrum. Methods Phys. Res., Sect. B **233**, 201 (2005).
[15] J. A. Tanis, J.-Y. Chesnel, B. Sulik, B. Skogvall, P. Sobocinski, A. Cassimi, J.-P. Grandin, L. Adoui, D. Hennecart, and N. Stolterfoht, Phys. Rev. A **74**, 022707 (2006).
[16] D. Misra, A. H. Kelkar, S. Chatterjee, and L. C. Tribedi, Phys. Rev. A **80**, 062701 (2009).
[17] J. L. Baran, S. Das, F. Járai-Szabó, K. Póra, L. Nagy, and J. A. Tanis, Phys. Rev. A **78**, 012710 (2008).
[18] K. Póra and L. Nagy, Nucl. Instrum. Methods Phys. Res., Sect. B **233**, 293 (2005).
[19] Double scattering is most pronounced when the two molecular atoms are aligned with the momentum of the incident particle and the emitted electron [8,27].
[20] M. Aymar, S. Azizi, and O. Dulieu, J. Phys. B **36**, 4799 (2003).
[21] http://www.nist.gov/pml/data/asd.cfm.
[22] D. Baye and P. H. Heenen, J. Phys. A **19**, 2041 (1986).
[23] V. S. Melezhik and D. Baye, Phys. Rev. C **59**, 3232 (1999).
[24] D. Baye, J. Phys. B **28**, 4399 (1995).
[25] L. F. Shampine and M. K. Gordon, *Computer Solution of Ordinary Differential Equations: The Initial Value Problem* (Freeman, San Fransisco, CA, 1975).
[26] The distribution ratio is convoluted with a Gaussian function, which allows a faster decaying of the ratio for higher momenta. A similar convolution procedure has been used in the work [29] to analyze the intramolecular decay.
[27] A. Messiah, *Quantum Mechanics* (North-Holland, Amsterdam, 1970), Vol. II, pp. 848–856.
[28] P. A. Lee and J. B. Pendry, Phys. Rev. B **11**, 2795 (1975).
[29] L. S. Cederbaum, J. Zobeley, and F. Tarantelli, Phys. Rev. Lett. **79**, 4778 (1997).